Computation & theory

Spatial pore distribution: an approach to uncouple the strength–porosity trade-offs

Prosenjit Biswas[1] and Ji Ma[1,*] (ORCID)

[1] Department of Materials Science and Engineering, University of Virginia, Charlottesville, VA 22904, USA

ABSTRACT

A spatial porosity distribution methodology is proposed to overcome the strength/porosity trade-offs in engineered porous materials. Stainless steel–316L structure produced through additive manufacturing with 18.53% overall porosity was shown to possess anisotropic stiffness from 7.40 to 150.18 GPa and compressive strength from 49.83 to 375.4 MPa depending on the spatial placement of porosity. This strategy broadens the range of accessible properties compared to controlling pore geometry. Computational tools have also been developed to quickly predict the stiffness and strength of the structure.

Springer

GRAPHICAL ABSTRACT
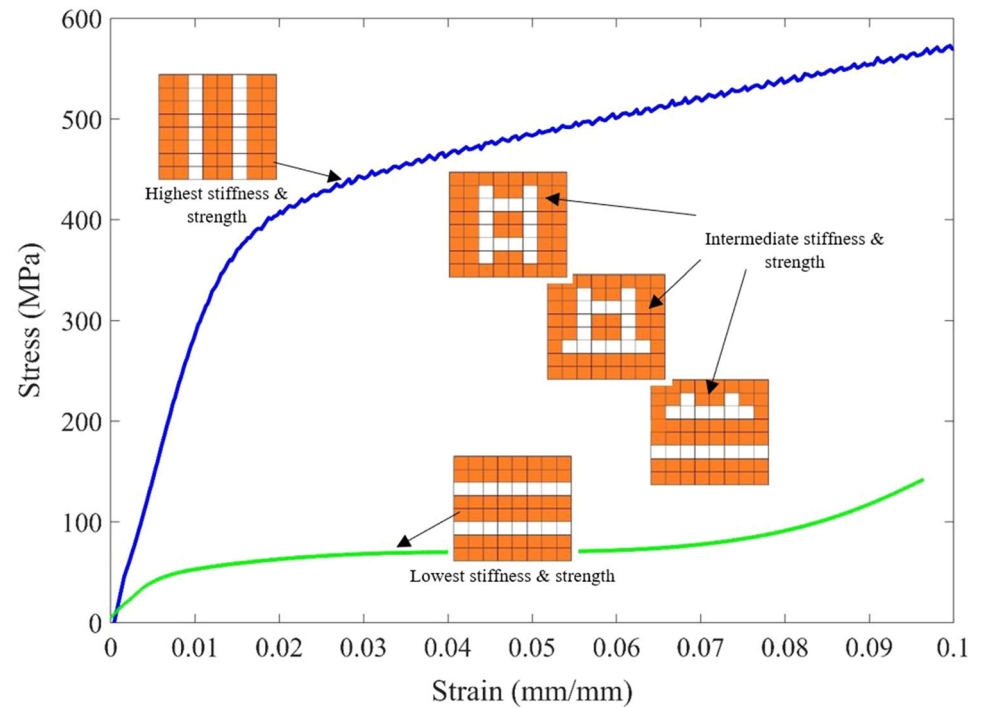
Introduction

Materials design has a significant impact on manufacturing and structural applications. However, there are often trade-offs in materials design. For example, strength–ductility and strength–porosity are competing factors, and a gain in one will be accompanied by the loss of the other [1–4]. Depending on the application, researchers have been intelligently applying these trade-offs in materials design to achieve the desired properties [5–7]. Generally, porous or lattice structures could be used to tailor the desired strength and stiffness below the solid component properties [8]. On the other hand, there are applications where it is desirable to maintain the overall porosity within a certain range. For instance, the overall porosity and pore size of medical implants play an important role in nutrients transportation and bone growth through the scaffolds [9]. Concurrently, the strength and stiffness of these scaffolds

need to be compatible with the human bone to reduce the stress shielding [10, 11]. As the porosity has a reciprocal impact on the stiffness/strength, simultaneously satisfying the requirements of porosity/pore size and strength/stiffness can be challenging. Lattice structures are often used to overcome this challenge by accessing a broader range of properties at a given level of porosity [8, 12–17]. However, the strut
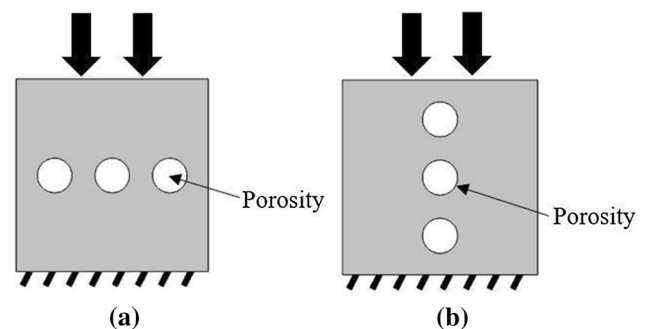

Figure 1 Spatial pore distribution of **a** parallel or lower bound geometry and **b** series or upper bound geometry.

architecture of these lattice geometries impacts the pore size/shape and can be a limiting factor for certain applications like cell growth and fluid transfer through biomedical implants [16, 18]. To de-couple the inverse relationship between strength/stiffness and porosity, we propose an approach of changing the spatial position of the porosity in this study. For example, by placing a fixed quantity of pores in different orientations, as shown in Fig. 1, the strength/stiffness of the sample could be modified along the loading direction without changing the porosity or the size/geometry of the pores. Metal additive manufacturing has been used to implement this concept of spatial pore distribution within the structure within this study.

Design of porous structure

Starting from a cube with dimensions of $(12 \times 12 \times 12)$ mm^3, as shown in Fig. 2a, we introduce porosity into this structure at certain locations. The solid cube is tessellated along (X, Y, Z) directions, turning the cube into an assembly of small cubic unit cells along with all three directions as shown in Fig. 2b. Each of these small cubes can be replaced by a lattice cell to define a desired porosity and porosity pattern. The resolution of the design domain can also be controlled by changing the tessellation spacing. In this study, porosity is assigned using a simple cubic lattice cell with dimensions $(1.5 \times 1.5 \times 1.5)$ mm^3 as shown in Fig. 3c. The strut dimension of this lattice cell is $(0.25 \times 0.25 \times 1.5)$ mm^3, which makes the cell porosity 74.1%. For simplicity, it is considered that each cell in the front face (XY plane) forms an array of similar cells along the thickness direction (Z). For example, the structure shown in Fig. 3 has two of the

eight layers along the height replaced by lattice cells (i.e., 25% of total cells are lattice cells). This makes the overall structural porosity 18.53%.

Spatial pore distribution (SPD) methodology

The advantage of this tessellated structure is the possibility to place and reorganize the lattice cells within the domain in any desired pattern to control the local geometrical properties. The solid and lattice cells are shown in their front view of the tessellated model, Fig. 4a, to resemble the porous structure in Fig. 3a. The orange color in Fig. 4 represents the solid cells, and the white color represents the lattice cells. Only the front face (XY plane face) is shown since an array of similar cells exists along the thickness direction (Z-direction shown in Fig. 2). While the lattice cells can be placed in any arbitrary location, Fig. 4 illustrates a set of patterns generated by moving two lattice cells from one row and placed in a column. Thus, from the beginning, Fig. 4a, to the end, Fig. 4g, the pore orientation is rotated by 90^0.

To estimate the stiffness and strength of these structures, the simple rule of mixtures (ROM) of composite materials can be used. In ROM, the composites can be represented using a parallel model (Voigt) and a series model (Reuss) [19] to obtain the upper and lower bounds, respectively. In the parallel model, the fiber directions are parallel to the loading direction and in the series model, the fibers are perpendicular to the loading direction. The models are expressed using the following equations:
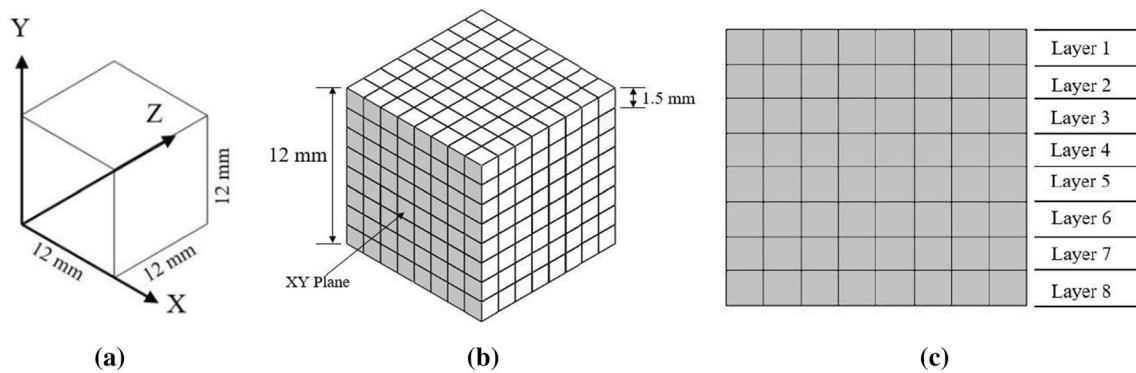
$$\text{Voigt model}: E_c^V = V_m E_m + V_f E_f \tag{1}$$

Figure 2 Geometry tessellation: **a** solid cube; **b** tessellated cube; **c** front face of the tessellated cube.
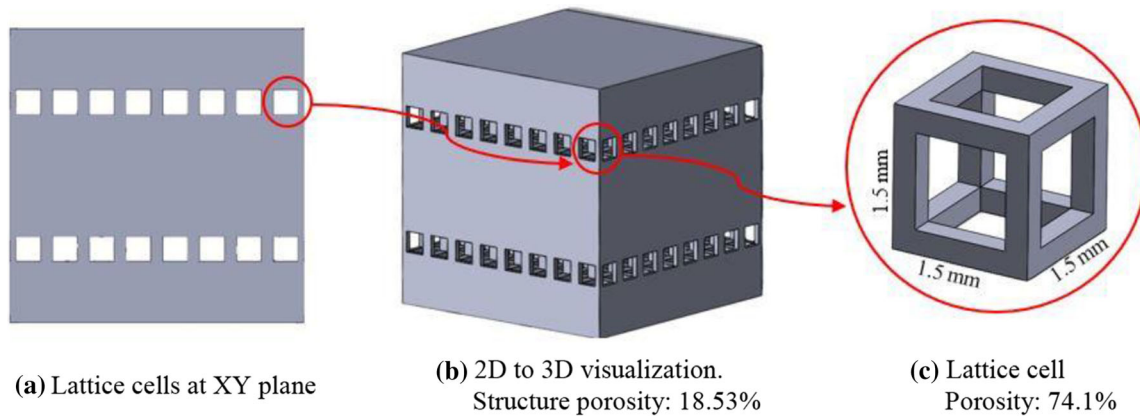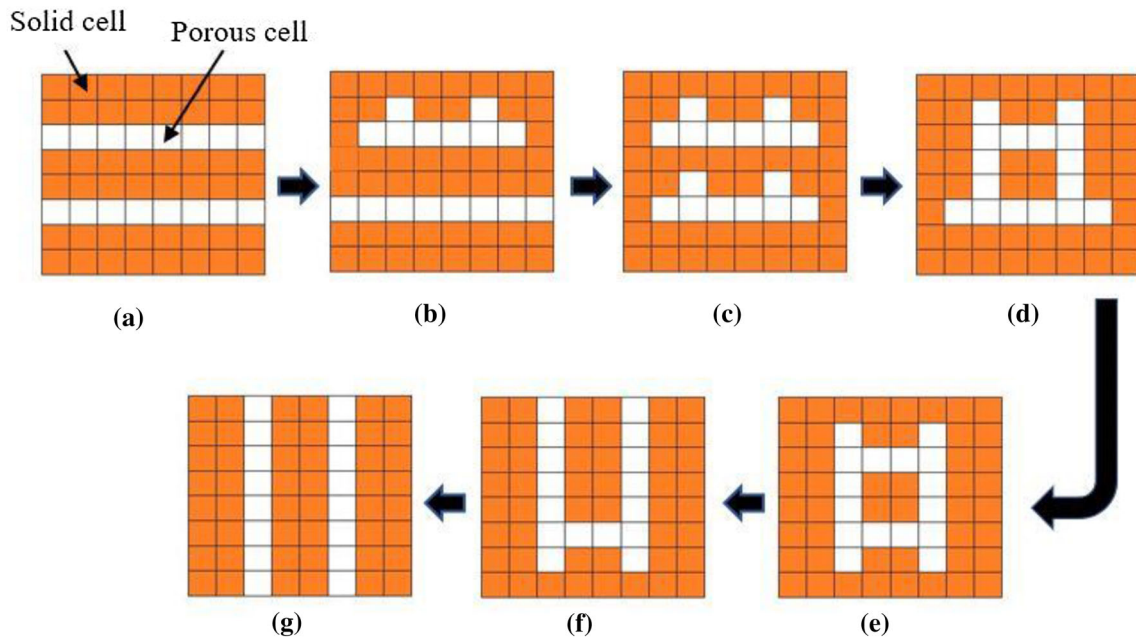
Figure 3 Design of porous structure.

Figure 4 Spatial pore distribution methodology.

Reuss model : $E_c^R = \dfrac{E_m E_f}{V_m E_f + V_f E_m}$ (2)

where E_c^V = stiffness of composite in Voigt (parallel) model.

E_c^R = stiffness of composite in Reuss (series) model

E_m and E_f = stiffness of matrix and fiber, respectively

V_m and V_f = volume fraction of matrix and fiber, respectively

In this study, since the lattice cells at the front face are considered to form an array of similar cells along the thickness direction, this array of lattice cells can be considered as a fiber. The stiffness of this fiber is
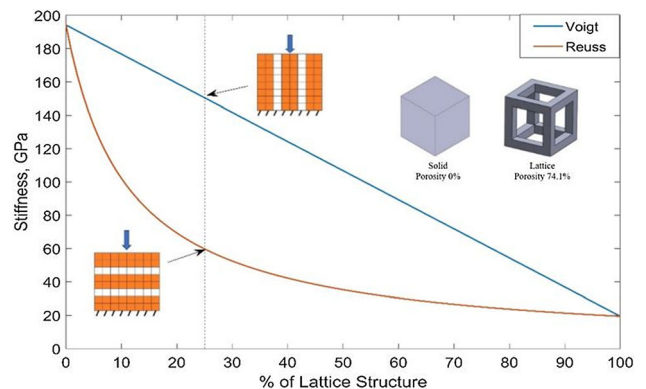

Figure 5 Stiffness bounds vs porosity relation in composites.

considered to be lower according to the load carrying area, i.e., with 74.1% porosity, the lattice cell has only 11.1% of the material stiffness. Figure 5 shows the variation of upper (Voigt) and lower (Reuss) stiffness bounds with the percentage of the lattice structure for the material SS-316L. The vertical dashed line dictates the achievable bounds and the pore orientation related to the highest and lowest stiffness when 25% of total cells are lattice cells, i.e., at 18.53% structural porosity.

Therefore, it is evident from Fig. 5 that for a vertical loading direction as shown, the pore orientation at Fig. 4a will have the lowest stiffness (59.74 GPa), and Fig. 4g will have the highest stiffness (150.5 GPa). The stiffness for all other pore orientations will fall within this bound. Since the lowest and highest stiffness in this technique is due to the pore orientation, the lowest stiffness structure, Fig. 4a, is named "compliant orientation (CO)" and the highest stiffness structure, Fig. 4g, is named as "rigid orientation (RO)."

Manufacturing of SPD structure

The lowest and highest stiffness models (CO and RO models) were additively manufactured (AM) from gas-atomized stainless steel 316L (SS-316L) powder using SLM Solutions 280 laser powder bed fusion machine (LBPF). The particle size (D_{50}) of the powder was 25 μm. The AM process parameters were set as shown in Table 1. All the samples were printed at 45^0 with the build plate to avoid print failure due to unsupported struts as shown in Fig. 6a. To avoid any damage to the fabricated lattice structures, samples were removed through the substrate via wire electro-discharge machining (wire EDM).

Table 1 Additive manufacturing process parameters

LPBF parameters	Values
Power	190 W
Scanning speed	750 mm/s
Hatch spacing	0.12 mm
Layer thickness	0.03 mm
Scan strategy	Stripes (67^0 rotation between layers)

Mechanical testing

Uniaxial compression tests were performed on the CO and RO structures along with two other additively manufactured solid cubes with dimension $(4 \times 5 \times 8)$ mm^3 using an MTS criterion model 43 (MTS-43) universal testing machine with 30-kN load capacity. Tests were performed at room temperature with a displacement rate of 0.005 mm/s, and the strain was measured directly with an extensometer attached to the sample. In cases where loads higher than 30kN were required, tests were conducted on an MTS-793 machine with a 100-kN load cell instead. In the MTS-793 machine, no extensometer was used due to the sample height constraints. For samples that required higher load, several tests were conducted on the MTS-43 load frame with the extensometer to obtain an accurate measurement of elastic modulus.

Computational tools to predict mechanical behavior

The arbitrary placement of porosity allows for myriad possible structures, and experimental characterization of every possible structure is not feasible. In this study, we propose two computational models to predict the properties of each possible structure.

Analytical modeling

The analytical model is beneficial to rapidly estimate the mechanical properties of any geometry. This technique divides the geometry into layers and gives freedom to model the stress and corresponding strain of individual layers through accessing the variation of layer area due to different pore distribution in each layer. This model is designed to predict the stiffness and yield strengths of any spatial pore distribution. However, it does not predict properties after the yield point, i.e., in the plastic region. The model simulates the result of a uniaxial compression experiment by evaluating the sample stress and sample strain at every load level.

Evaluation of stress The overall stress is found by $\sigma = F/A$, where the F is the applied force and A is the cross-sectional area of the $12 \times 12 \times 12$ mm^3 solid cube. This will provide the engineering stress value of the whole geometry to obtain the stress–strain behavior. To obtain the incremental stresses, the
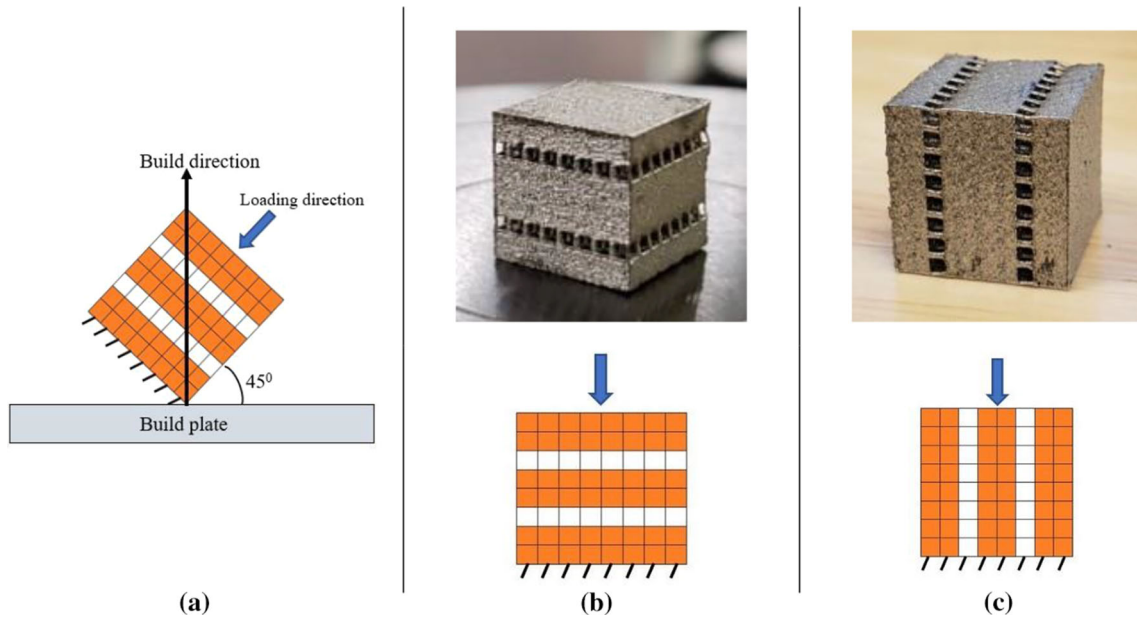
Figure 6 3D printing orientation and printed samples: **a** illustration of printing orientation; **b** compliant orientation (CO); and **c** rigid orientation (RO).

applied force, F, has been divided into q number of steps keeping the cross-sectional area, A constant. Thus, the incremental force for each step, F', can be represented as :

$$F' = \frac{F}{q} * i \text{ where } i = 1, 2, 3, \ldots q \quad (3)$$

The stress on the structure for each incremental force, F', can be represented by:

$$\sigma' = \frac{F'}{A} = \frac{\frac{F}{q} * i}{A} \quad (4)$$

Thus, the incremental stresses can be obtained for the geometry. Now, to plot the stress–strain response of the whole geometry, the strain corresponding to each incremental stress needs to be evaluated, which is discussed in the following section.

Evaluation of Strain Ramberg–Osgood model [20] is used in this study to evaluate the strain, ε', of the geometry for each incremental stress, σ'. This model is often used to describe the nonlinear stress–strain behavior of ductile metals by expressing the stress as a function of total strain. Although it shows excellent agreement with experiments below the yield point, it sometimes overestimates the stress in the plastic region [21]. Moreover, the current study deals with porous geometry, where the porosity distribution can also vary with the height of the structure as shown in

Fig. 4a–g. To use the Ramberg–Osgood model for porous structure, the model needs to be adjusted to normalize the effect of porosity. The technique of geometry tessellation mentioned in "Design of porous structure" section can overcome this issue. Taking Fig. 4a as an example, the tessellation has divided the whole structure into eight layers along with the height (Fig. 7) and it is also evident that the load-carrying area of each layer (a^L) can be different. As seen from Fig. 7, layers 3 and 6 have smaller load-carrying area than the other layers, since those layers are replaced by the lattice cells.

Considering the actual area of each layer for incremental force, F', the stress experienced by the material in each layer (σ') is also different. The Ramberg–Osgood model can be used to calculate the
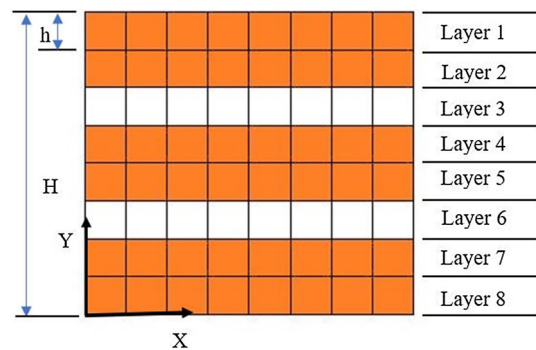

Figure 7 Variation of layer area.

strain of that layer. The displacement of each layer can be found by multiplying the strain of that layer with the layer thickness. Summing the displacement from all layers, the total displacement of the entire sample is obtained. Finally, the strain of the geometry can be evaluated for corresponding σ' by dividing the total sample displacement by the sample height. The detailed procedure to evaluate the overall strain from the actual layer area is discussed below:

Calculating layer stress Let the tessellation produces m number of layers along with height (Y direction) and the effective layer area is a^L. Now, the actual area of each layer can be calculated using :

$$a_j^L = B\left[(R - V_j)A_s + V_j A_v\right], \text{ where } j = 1, 2, 3, \ldots m \tag{5}$$

$$\text{Actual layer stress}, \sigma_j^L = \frac{F'}{a_j^L} \tag{6}$$

where B = Total number of cells along the thickness direction (Z dir).

R = Total number of cells along the width (X dir)

V_j = Number of lattice cells in a layer

A_s = Area of the solid cells

A_v = Area of the void cells

Calculating layer strain and displacement The Ramberg–Osgood model is used to calculate the layer strain, ε_j^L, corresponding to the F' using the following equation:

$$\varepsilon_j^L = \frac{\sigma_j^L}{E} + 0.002 * \left[\frac{\sigma_j^L}{E_y}\right]^n \tag{7}$$

$$\varepsilon_j^L = \frac{F'}{a_j^L * E} + 0.002 * \left[\frac{F'}{a_j^L * \sigma_y}\right]^n \tag{8}$$

where n = strain hardening = $\frac{log(20)}{log(\frac{\sigma_{0.2}}{\sigma_{0.01}})}$

E = Young's modulus of the material

σ_y = Yield strength of the material.

Now, the displacement of each layer, $D_j^L = \varepsilon_j^L * h$, where h = height of each layer.

Total displacement and strain of the geometry The displacement from each layer can be added all together to get the overall displacement of the geometry.

$$\text{Total displacement}, D' = \sum_{j=1}^{m} \varepsilon_j^L * h \tag{9}$$

The total strain of the geometry corresponding to F', $\varepsilon' = \frac{D'}{H} = \sum_{j=1}^{m} \frac{\varepsilon_j^L * h}{H}$, where H = height of the geometry. Therefore, by plotting (σ', ε') and (F', D'), both the stress–strain and force–displacement curve can be achieved.

Finite element analysis

To simulate the deformation behavior of the porous structures, finite element analysis was performed using ANSYS workbench software. Boron carbide (E = 441 GPa and v = 0.17 [22]) is used as platen material, and SS-316L is used for the SPD geometry. The material properties of SS-316L are obtained as E = 194.16 GPa, σ_y = 603.5 MPa and v = 0.31 from the solid cube tested. For all the FE models, 4-node tetrahedral-type 3D solid elements were employed to mesh the SPD geometry. Convergence studies were conducted for a range of mesh sizes to determine the mesh size of 0.5 mm for the SPD geometry. Boundary conditions are also followed from the experiments, in which compression loadings are applied on the platens at the top of the geometry and the bottom of the geometry is fixed in all three directions. Bonded contact type was defined between the platen and the SPD geometry. To construct the stress–strain curve, the displacement of a node has been extracted from the top surface of the sample. The extracted displacement from the node has incremental displacement values for each incremental step till the final displacement of the structure. These displacement values are then divided by the total height of the geometry to get the respective strain. To obtain the stress values corresponding to the strain of each step, the applied load has been divided into the same number of steps as the finite element and divided by the cross-sectional area of the (12 × 12 × 12) mm^3 solid cube.

Results and discussion

Experimental results

The engineering stress–strain behavior of the 3D-printed CO and RO models from the experimental analysis is shown in Fig. 8. The stiffness of CO and
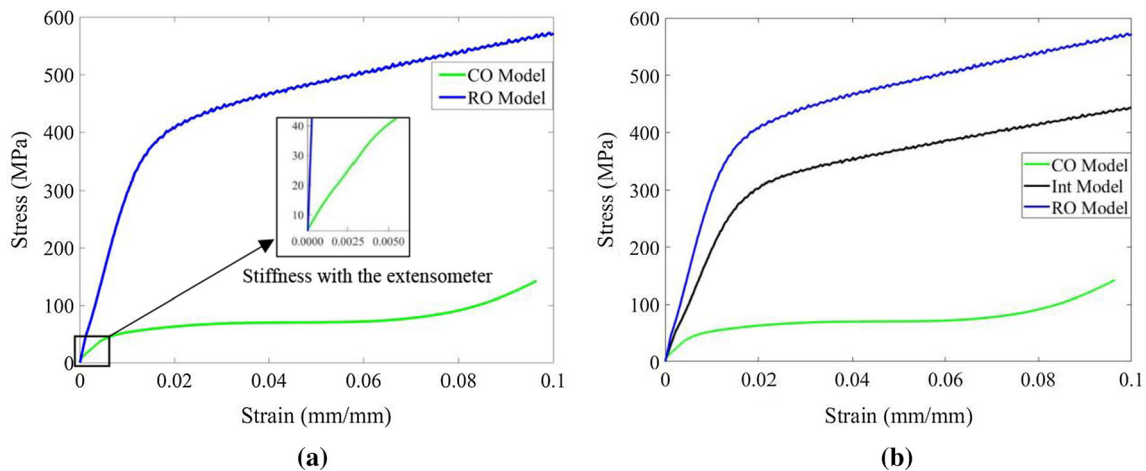
Figure 8 a Engineering stress–strain curve of the CO and RO model with magnified inset to better show the stiffness differences; **b** engineering stress–strain curves of the Int model compared to the CO and RO models.

Table 2 Comparison between experimental and computational results

Method	Model					
	CO model		Int model		RO model	
	E (GPa)	σ_y (MPa)	E (GPa)	σ_y (MPa)	E (GPa)	σ_y (MPa)
Experimental	7.40	49.83	96.30	280.3	150.18	375.4
Theoretical	64.73	68.08	144.61	347.2	151.01	465.3
FEA	63.24	71.18	109.83	324.1	132.48	486.1
ROM	59.74	–	–	–	150.5	–

RO models is calculated from the elastic part, and the yield strength of these models has been determined using the 0.2% strain offset method. The stiffness and yield strength of the CO models are found to be 7.4 GPa and 49.83 MPa, and for RO models, it is 150.18 GPa and 375.4 MPa, respectively. The stiffness is closely aligned with the rule of mixture predictions in "Spatial pore distribution (SPD) methodology" section. Properties within this bounded range can be accessed easily using the other spatial pore orientations combination. In other words, the SPD orientations in Fig. 4b–f should exhibit material properties within this range. Moreover, the AM printed parts can exhibit anisotropic mechanical properties depending on building orientation [23, 24]. To verify these, the results from the printed solid cubes, one having the build direction parallel to the loading direction and the other one with the build direction perpendicular to the loading direction, were compared. Only minor strength variation ($\sim$ 4.05%) was observed, compared to the variations from the SPD orientations (653.4%).

Hence, the impacts of printing conditions are not taken into consideration in this study.

Computational results and validation

Table 2 shows the comparison of all the computational results (theoretical, FEA and ROM) with the experimental results for both the CO and RO models. The stiffness and strength from both the theoretical and FEA predictions are in good agreement with each other. Compared to experimental results, the model predictions of the RO model are reasonable, but the prediction for the CO model is poor. This is caused by a combination of geometrical imperfections of the printed sample and elastic instabilities of the structure.

In the CO model, the highest stresses occur within the lattice struts as can be seen from Fig. 6b. Since the SPD samples were printed 45^0 aligned with the building direction (Fig. 6a), some of the lattice struts warped slightly due to high residual stresses developed in these regions. This is especially visible along

Figure 9 **a** Figure showing the as-printed samples of the CO model and **b** the CO model after deformation.
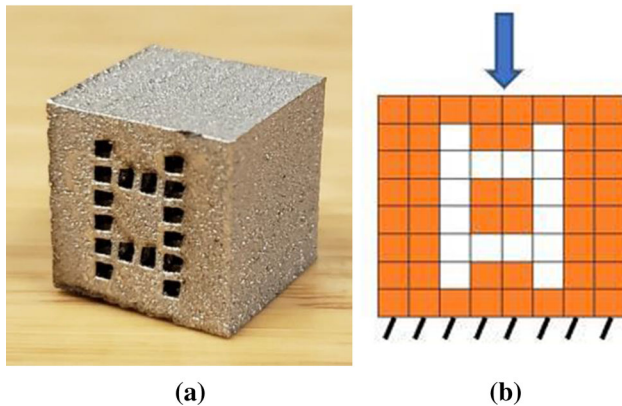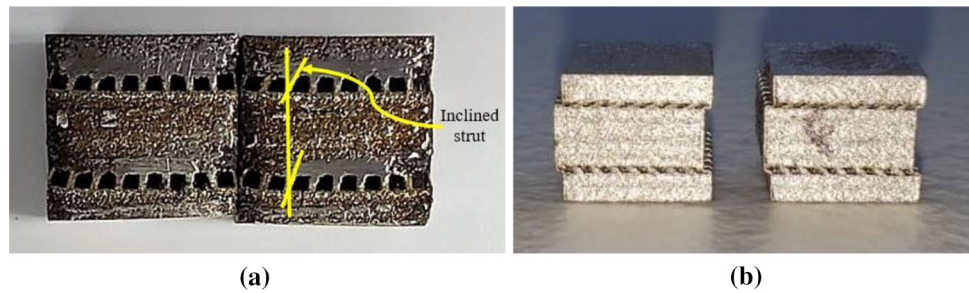
(a)

(b)

(a)   (b)

Figure 10 **a** As-printed Int model and **b** illustration showing loading direction.

the surface (Fig. 9a). Because of these inclined struts, instead of carrying the load in pure compression, it carries the load in bending like an inclined cantilever, which causes the deformation to take the form of Fig. 9b, where the middle portion is sheared. This reduces both the stiffness and yield strength of the structure (Fig. 6b).

Discussion

The computational tools developed in this study are designed to predict the properties from any other combinations of pore distribution are bounded by the properties shown by CO and RO models. To verify this, an intermediate (Int) SPD orientation (Fig. 4e) is chosen and additively manufactured (Fig. 10) using the same process parameters as mentioned in Table 1.

The full-range stress–strain behavior of the Int model is shown in Fig. 8b. The comparison of experimental and computational results is shown in Table 2. As expected, the properties fall between the CO and RO models. The strength found through the experiment is about 13.5% lower than the FEA model predictions and 19.2% lower than the theoretical model predictions. On the other hand, the model-predicted stiffness is significantly higher than the experimental results. This is caused by the bending of inclined struts that was also responsible for lower experimental stiffness in the CO model.

Overall, the current study shows that using the proposed SPD technique it is possible to hold the overall porosity of a structure constant, while the strength of the structure can be significantly varied. An important feature of this technique is any properties within the range of the minimum and maximum accessible mechanical properties, depending on the material used, can be accessed easily through engineering the spatial pore distribution.

To explore whether the SPD technique can be advantageous by accessing a broader range of properties than the different lattice cell strategies, studies for different lattice cell geometries are compared with SPD. The theoretical range for maximum and minimum mechanical properties can be evaluated using the rule of mixture equations for any given material at any porosity level. For each material, there is an upper and lower bound value at a given porosity. However, the exact values depend on the material. Therefore, to compare among different materials, the upper and lower bound values range is normalized and reported as 0% (lower bound value) to 100% (upper bound value).

Several studies [8, 25, 26] discussed the impact of lattice cell geometry on the mechanical properties of scaffolds and are compared with the SPD technique of this paper. The comparison between these studies and SPD is shown in Fig. 11. For example, Roohani-Esfahani et al. [8] study the effects of lattice geometry on the compressive strength of a strontium-hardys-tonite-gahnite (Sr-Ht-Ga) lattice while holding porosity constant. At 70% porosity, the accessible range of properties by changing the lattice type (from rectangular to hexagonal lattice) was 41–69% of upper bound values. Similarly, separate studies [25, 26] on the effects of lattice cell geometry of Ti-

Figure 11 Achievable property range comparison.
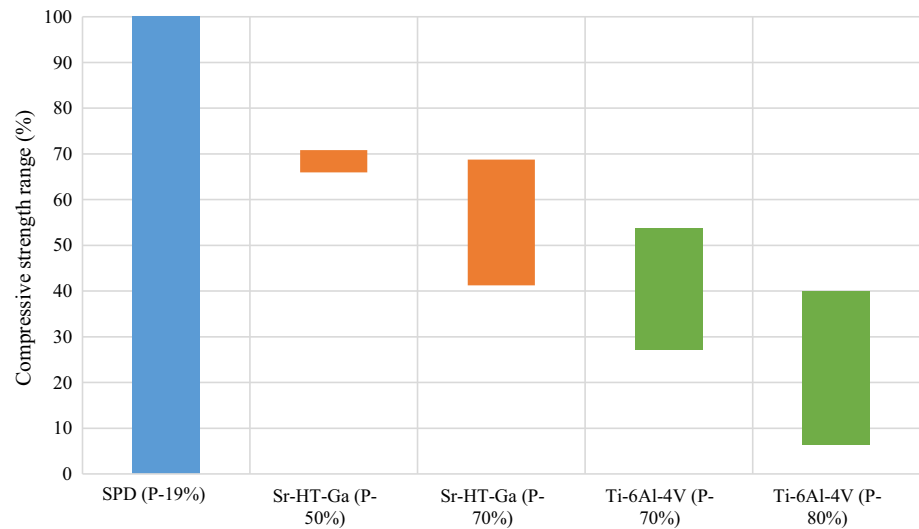
6Al-4V lattices showed that the compressive strength could be tuned between 27 and 53% on the upper bound value by changing from rectangular strut to diagonal strut. Ashby charts summarized by Dong et al. [27] show that even when the range of possible lattice geometry is expanded, for example, to include octet lattices and elastic buckling-dominated structures, it is not possible to fully cover the entire range of properties between upper and lower bounds at a given porosity or material density. On the other hand, as evident from this study, through spatial pore distribution technique, it is possible to access any desired properties within the accessible range. It is noteworthy that the SPD technique provides highly anisotropic properties—moreso that the anisotropic response observed in lattice structures.

Conclusion

An approach of spatial pore distribution (SPD) technique is proposed in this study to uncouple the strength–porosity relation of materials. The SPD technique provides the freedom to access any specific location within geometry and thereby very helpful to engineer the local and global mechanical properties of a porous structure while holding the overall porosity constant. To implement this technique SS-316L samples were additively manufactured and compression tested to assess the variations of stiffness and strengths with different pore distributions. The results showed that the SPD technique can provide a significantly broader range of stiffness and strength properties compared to the lattice cell geometry variations. Furthermore, SPD can access any properties within this range. With this ability to tailor the mechanical properties of porous structure keeping the overall porosity constant, the SPD technique can be used to uncouple the strength/porosity trade-off of materials and it undoubtedly adds a new degree of freedom to the part design. However, the resultant structures are highly anisotropic and are sensitive to structural defects created during the additive manufacturing process.

References

[1] Ma E, Zhu T (2017) Towards strength–ductility synergy through the design of heterogeneous nanostructures in metals. Mater Today 20:323–331. https://doi.org/10.1016/j.mattod.2017.02.003

[2] Yinmin W, Mingwei C, Fenghua Z, En M (2002) High tensile ductility in a nanostructured metal. Nature 419:912. https://doi.org/10.1038/nature01133

[3] Meyers MA, Mishra A, Benson DJ (2006) Mechanical properties of nanocrystalline materials. Prog Mater Sci 51:427–556. https://doi.org/10.1016/j.pmatsci.2005.08.003

[4] Liu P, Fu C, Li T, Shi C (1999) Relationship between tensile strength and porosity for high porosity metals. Sci China Ser

E Technol Sci 42:100–107. https://doi.org/10.1007/BF02917065

[5] Lu K (2014) Making strong nanomaterials ductile with gradients. Science 345:1455–1456. https://doi.org/10.1126/science.1255940

[6] Kumar KS, Van Swygenhoven H, Suresh S (2003) Mechanical behavior of nanocrystalline metals and alloys. Acta Mater 51:5743–5774. https://doi.org/10.1016/j.actamat.2003.08.032

[7] Li F, Xue X, Jia T, Dang W, Zhao K, Tang Y (2020) Lamellar structure/processing relationships and compressive properties of porous Ti6Al4V alloys fabricated by freeze casting. J Mech Behav Biomed Mater 101:103424. https://doi.org/10.1016/j.jmbbm.2019.103424

[8] Roohani-Esfahani SI, Newman P, Zreiqat H (2016) Design and fabrication of 3D printed scaffolds with a mechanical strength comparable to cortical bone to repair large bone defects. Sci Rep 6:1–8. https://doi.org/10.1038/srep19468

[9] Bose S, Vahabzadeh S, Bandyopadhyay A (2013) Bone tissue engineering using 3D printing. Mater Today 16:496–504. https://doi.org/10.1016/j.mattod.2013.11.017

[10] Yang F, Chen C, Zhou Q, Gong Y, Li R, Li C, Klämpfl F, Freund S, Wu X, Sun Y, Li X, Schmidt M, Ma D, Yu Y (2017) Laser beam melting 3D printing of Ti6Al4V based porous structured dental implants: fabrication, biocompatibility analysis and photoelastic study. Sci Rep 7:1–12. https://doi.org/10.1038/srep45360

[11] Gross S, Abel EW (2001) A finite element analysis of hollow stemmed hip prostheses as a means of reducing stress shielding of the femur. J Biomech 34:995–1003. https://doi.org/10.1016/S0021-9290(01)00072-0

[12] Ahmadi SM, Yavari SA, Wauthle R, Pouran B, Schrooten J, Weinans H, Zadpoor AA (2015) Additively manufactured open-cell porous biomaterials made from six different space-filling unit cells: the mechanical and morphological properties. Materials (Basel) 8:1871–1896. https://doi.org/10.3390/ma8041871

[13] Dumas M, Terriault P, Brailovski V (2017) Modelling and characterization of a porosity graded lattice structure for additively manufactured biomaterials. Mater Des 121:383–392. https://doi.org/10.1016/j.matdes.2017.02.021

[14] Gupta A, Talha M (2015) Recent development in modeling and analysis of functionally graded materials and structures. Prog Aerosp Sci 79:1–14. https://doi.org/10.1016/j.paerosci.2015.07.001

[15] Mehrali M, Shirazi FS, Mehrali M, Metselaar HSC, Bin Kadri NA, Osman NAA (2013) Dental implants from functionally graded materials. J Biomed Mater Res Part A 101:3046–3057. https://doi.org/10.1002/jbm.a.34588

[16] Mullen L, Stamp RC, Brooks WK, Jones E, Sutcliffe CJ (2009) Sutcliffe, Selective laser melting: A regular unit cell approach for the manufacture of porous, titanium, bone in-growth constructs, suitable for orthopedic applications. Biomed Mater Res Part B Appl Biomater 89:325–334. https://doi.org/10.1002/jbm.b.31219

[17] Wang L, Kang J, Sun C, Li D, Cao Y, Jin Z (2017) Mapping porous microstructures to yield desired mechanical properties for application in 3D printed bone scaffolds and orthopaedic implants. Mater Des 133:62–68. https://doi.org/10.1016/j.matdes.2017.07.021

[18] Ali D, Sen S (2017) Finite element analysis of mechanical behavior, permeability and fluid induced wall shear stress of high porosity scaffolds with gyroid and lattice-based architectures. J Mech Behav Biomed Mater 75:262–270. https://doi.org/10.1016/j.jmbbm.2017.07.035

[19] N.L. Hancox, Engineering mechanics of composite materials, 1996. https://doi.org/10.1016/s0261-3069(97)87195-6.

[20] Ramberg W, OsgoodWR (1943) Description of stress-strain curves by three parameters. Technical Note No. 902, National Advisory Committee for Aeronautics

[21] Abdella K (2006) Inversion of a full-range stress-strain relation for stainless steel alloys. Int J Non Linear Mech 41:456–463. https://doi.org/10.1016/j.ijnonlinmec.2005.10.002

[22] Thévenot F (1990) Boron carbide-a comprehensive review. J Eur Ceram Soc 6:205–225. https://doi.org/10.1016/0955-2219(90)90048-K

[23] Mukherjee M (2019) Effect of build geometry and orientation on microstructure and properties of additively manufactured 316L stainless steel by laser metal deposition. Materialia 7:5–8. https://doi.org/10.1016/j.mtla.2019.100359

[24] Alsalla HH, Smith C, Hao L (2018) Effect of build orientation on the surface quality, microstructure and mechanical properties of selective laser melting 316L stainless steel. J Clean Prod. https://doi.org/10.1108/RPJ-04-2016-0068

[25] Barui S, Chatterjee S, Mandal S, Kumar A, Basu B (2017) Microstructure and compression properties of 3D powder printed Ti-6Al-4V scaffolds with designed porosity: experimental and computational analysis. Mater Sci Eng C 70:812–823. https://doi.org/10.1016/j.msec.2016.09.040

[26] Ataee A, Li Y, Fraser D, Song G, Wen C (2018) Anisotropic Ti-6Al-4V gyroid scaffolds manufactured by electron beam melting (EBM) for bone implant applications. Mater Des 137:345–354. https://doi.org/10.1016/j.matdes.2017.10.040

[27] Dong L, Deshpande V, Wadley H (2015) Mechanical response of Ti-6Al-4V octet-truss lattice structures. Int J Solid Struct 60–61:107–124. https://doi.org/10.1016/j.ijsolstr.2015.02.020